The Journal of Physical Chemistry Letters

Letter

Cite This: J. Phys. Chem. Lett. 2018, 9, 1018−1027

pubs.acs.org/JPCL

Electro-optic Response in Germanium Halide Perovskites

Grant Walters and Edward H. Sargent*

Department of Electrical and Computer Engineering, University of Toronto, 35 St. George Street, Toronto, Ontario M5S 1A4, Canada

Supporting Information

ABSTRACT: Electro-optic materials that can be solution-processed and provide high-crystalline quality are sought for the development of compact, efficient optical modulators. Here we present density functional theory investigations of the linear electro-optic coefficients of candidate materials cesium and methylammonium germanium halide perovskites. As with their lead halide counterparts, these compounds can be solution-processed, but in contrast, they possess the noncentrosymmetric crystal structures needed to provide a linear electro-optic effect. We find substantial electro-optic responses from these compounds; in particular, for the r_{51} tensor element of $CsGeI_3$, we predict an electro-optic coefficient of 47 pm·V^{-1} at the communications wavelength of 1550 nm, surpassing the strongest coefficient of $LiNbO_3$ at 31 pm·V^{-1}. The strong electro-optic responses of the germanium compounds are driven by high nonlinear susceptibilities and dynamics of the germanium atoms that ultimately arise from the distorted crystal structures. Alongside the electro-optic coefficient calculations, we provide the frequency responses for the linear and nonlinear electronic susceptibilities.

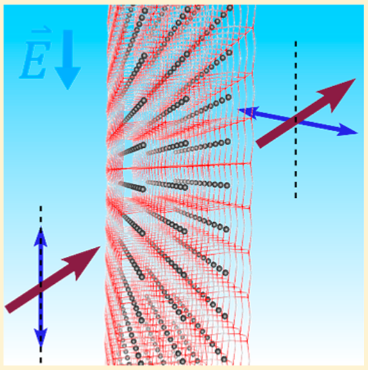

The development of efficient, compact electro-optic modulators for use in intrachip or interchip optical interconnects will be further advanced by expanding the set of electro-optic materials options. Established inorganic crystals, chiefly $LiNbO_3$ and $BaTiO_3$, are fabricated using processing techniques, such as Czochralski crystal growth or epitaxial MOCVD, that limit compatibility with standard silicon photonics. Organic materials are deposited via inexpensive and simple solution-processing methods and have performed impressively when incorporated within pioneering modulator architectures such as silicon slot-waveguide interferometers.[1,2] Unfortunately, the electrostatic poling of the organic molecules that is needed to orient and maintain orientation of the molecules has limited their breadth of application to date.

These limitations motivate the search for new solution-processed materials that exhibit strong, built-in, electro-optic activity.

Recently, metal halide perovskites have risen as solution-processed materials with impressive electrical and optical properties. These materials, possessing the chemical formula ABX_3 (where A is a cation, B is a metal cation, and X is a halide anion), have demonstrated impressive performance in a broad range of optoelectronic devices.[3−6] Elements of the success of metal halide perovskites can be traced to their flexibility in composition and morphology. The optical, electrical, and structural properties can be finely tuned through different combinations of cations and anions.[7,8] Various solution-processing methods can be used to grow different forms of perovskites: quantum-confined nanostructures,[9−11] polycrystalline thin films,[12] and macroscopic single crystals.[13,14]

The nonlinear optical properties are much less explored than their behavior as light-absorbing and light-emitting materials. The widely researched metal halide perovskites, particularly the lead-based ones, are structurally globally centrosymmetric and therefore are incapable of some nonlinear optical processes, including the linear electro-optic (LEO) effect.

The germanium halide perovskites are a class of non-centrosymmetric compounds. As in the case of lead, germanium is a group IV element that is capable of carrying a 2+ valence state. However, its higher position within the periodic column lends the 4s electron pair greater stereochemical activity when compared to the lead analogue.[15] This activity distorts the perovskite unit cell, causing it to lose its inversion symmetry. The germanium halide perovskites are drawing increased interest as lead-free alternatives for photovoltaic application[16−19] and have also previously been reported to exhibit impressive second-harmonic generation (SHG),[20−24] a phenomenon intimately linked with LEO. Motivated by this fact, combined with their transparency over the infrared communications wavelengths[20,25,26] and evidence for growth of crystals from solution,[20,22,23,25,27,28] we investigate herein the electro-optic and nonlinear optical behavior for germanium halide perovskites using density functional theory calculations.

We focus our study on cesium germanium halides ($CsGeX_3$; X = I, Br, Cl) and methylammonium germanium iodide ($MAGeI_3$). We provide predictions for the LEO coefficients and, by examining the factors contributing to the electro-optic behavior and the trends associated with the halide anions and A cations, provide mechanistic insights into the LEO responses. We complement these predictions with calculations of the

Received: December 19, 2017
Accepted: February 9, 2018
Published: February 9, 2018

linear and nonlinear susceptibilities and their frequency responses.

As in other metal halide perovskites, germanium-based perovskites assemble as an inorganic network of metal halide octahedra surrounding their A-site cations, such as methylammonium or cesium cations. However, in contrast with most other perovskites, those based on germanium have a distorted unit cell: they reside in the noncentrosymmetric trigonal $R3m$ space group.[20,22,23,27,29] The rhombohedral representation of the crystal structure is provided in Figure 1a−c. The angular lattice parameter of the unit cell deviates only slightly from 90°. The A cations occupy the corners, the halide species occupy positions near the face centers, and the germanium atoms occupy positions offset along the [111] direction from the body centers. For compounds with the polar molecular methylammonium, which possesses C_{3v} symmetry, the molecule's C−N axis aligns along the [111] direction.[20] The atomic offsets yield two distinct Ge−X bonds. Notably, the central offset of the germanium cations is reminiscent of that for titanium atoms in the electro-optic material $BaTiO_3$.

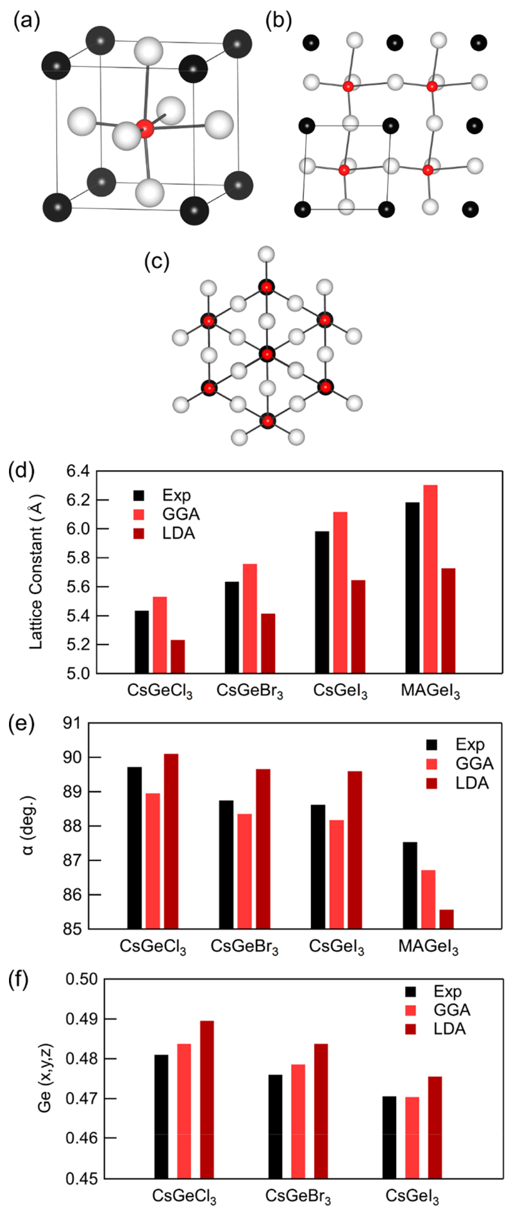

Figure 1. Structural representations of the rhombohedral lattice for germanium halide perovskites: (a) standard orientation, (b) [100] view, (c) [111] view showing hexagonal symmetry. Red, black, and white spheres are Ge^{2+} cations, A^+ cations, and X^- halide anions, respectively. Calculated structural parameters: (d) lattice constant, (e) lattice angular parameter, (f) XYZ coordinate of the near-body-center Ge atoms. Experimental results are taken from refs 20 and 22.

Calculations of the structural parameters (Figure 1d−f and Table S1) agree with the experimental findings for synthesized microcrystals.[20,22,23,27,29] Unsurprisingly, the cesium compounds show that as the size of the halide anion increases, the unit cell expands. The unit cell's angular deviation grows as the cell expands. $MAGeI_3$ has a similar lattice constant as its cesium counterpart, but it exhibits a much greater angular distortion. The germanium atoms' offset from the body-center increases as the halide size increases. Accompanying this is a change in the offset of the halide species from the face-centers that lessens the discrepancy between the two lengths of Ge−X bonds.

Electro-optic materials, to be of use in optical communications systems, are required to be optically transparent across the infrared communications bands. As in the case of most metal halide perovskites, the electronic bandgaps of the germanium compounds decrease as the halide size increases and lie within the visible spectrum. Substitution of cesium cations with methylammonium leads to widening of the bandgap, which has previously been attributed to further stereochemical activition of the germanium $4s^2$ lone pair.[20]

We calculated the bandgaps at the levels of the LDA, GGA, and HSE06 approximations (Table 1). We further calculated the real and imaginary components of the dielectric function, $\varepsilon(\omega)$, at optical frequencies (atomic positions are clamped) at the LDA level using scissors corrections set to the experimentally reported bandgaps; the response curves are provided in Figure 2. The use of scissors corrections is necessary due to the problem of bandgap underestimation in DFT and the consequent overestimation of the dielectric properties.[21,30,31] The corrections act as rigid shifts to the conduction bands in order to curtail bandgap estimation and have been widely used in calculations of linear and nonlinear optical properties of many materials.[21,30−46] As empirical adjustments, these corrections introduce a degree of uncertainty to the calculations; however, as we show below, these corrections are validated by the strong agreement between the scissors-corrected and experimental SHG characteristics.

Table 1. Calculated Bandgap Values (eV)

compound	LDA	GGA	HSE06	exp.
$CsGeCl_3$	2.01	2.21	2.22	3.43[a]
$CsGeBr_3$	1.26	1.53	1.66	2.38[a]
$CsGeI_3$	0.66	1.19	1.41	1.6[b]
$MAGeI_3$	0.37	1.52	1.84	1.9[b]

[a]Reference 22. [b]Reference 20.

The germanium materials possess uniaxial birefringence and refractive indices that scale with bandgap. Along with the dielectric functions, we have plotted the electronic band structures in Figure 3. All of the germanium compounds exhibit a direct bandgap at the Brillouin zone Z point; the rhombohedral nature of these crystals changes the gap from the R point of cubic perovskite phases.[47] The first few optical

DOI: 10.1021/acs.jpclett.7b03353
J. Phys. Chem. Lett. 2018, 9, 1018−1027

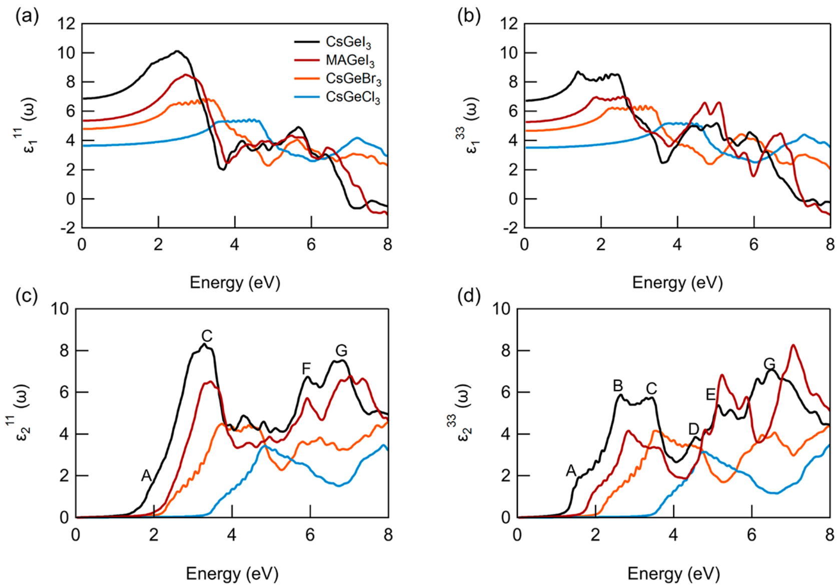

Figure 2. Calculated dielectric functions for germanium halide perovskites. (a) Real ordinary components. (b) Real extraordinary components. (c) Imaginary ordinary components. (d) Imaginary extraordinary components. Lettering on the curves for $CsGeI_3$ is used to connect with the electronic band dispersion plot. Calculations have been done with LDA exchange−correlation functionals and have been scissors-corrected.

transitions can be connected with spectral features in the imaginary dielectric functions.

The LEO effect is the special case of second-order nonlinear optical processes where one of the interacting electric fields is low-frequency while the other remains at optical frequencies. Changes to the optical dielectric constants can be induced by the low-frequency electric fields and are related through LEO coefficients. The LEO effect on the optical dielectric constant is defined by the following relation

$$\Delta(\varepsilon^{-1})_{ij} = \sum_{\gamma=1}^{3} r_{ij\gamma}E_\gamma \tag{1}$$

where $r_{ij\gamma}$ are the LEO coefficients and E_γ are electric field components (Greek indices correspond to static directional fields, and Latin indices correspond to optical directional fields). The LEO coefficients are the central figures of merit for electro-optic materials; a large LEO coefficient is key for efficient electro-optic modulation. The LEO coefficients of a material can be calculated with density functional perturbation theory (DFPT), as formulated by Veithen et al.[30] By determining the energetic changes induced by atomic displacements and homogeneous electric fields using DFT calculations, the electro-optic coefficients can be found.

The LEO coefficients at telecommunications bandwidths (i.e., field frequencies above 100 MHz) are formed from two contributions: an electronic, $r^{\text{el}}_{ij\gamma}$, and an ionic, $r^{\text{ion}}_{ij\gamma}$, response.[30] Within the Born−Oppenheimer approximation, these two quantities sum to form the total LEO coefficient. The electronic contribution is due to field interactions with the valence electrons while considering the ions as clamped. This term is related to the LEO second-order susceptibility, $\chi^{(2)}_{ijk}(-\omega;\omega,0)$, via

$$r^{\text{el}}_{ij\gamma} = \frac{8\pi}{n_i^{\,2} n_j^{\,2}} \chi^{(2)}_{ijk}(-\omega;\,\omega,\,0)\Big|_{k=\gamma} \tag{2}$$

where n are refractive indices.[30] We note that the DFT calculations of this term neglect the dispersion of the second-order susceptibility, and therefore, the term typically presents a lower bound. The ionic contribution accounts for the relaxation of the atomic positions due to the electric field and the corresponding dielectric changes. This term is given by a sum over the transverse optic phonon modes (indexed by m)

$$r^{\text{ion}}_{ij\gamma} = -\frac{4\pi}{\sqrt{\Omega_0}\, n_i^{\,2} n_j^{\,2}} \sum_m \frac{\alpha^m_{ij} p_{m,\gamma}}{\omega_m^{\,2}} \tag{3}$$

where Ω_0 is the unit cell volume, α^m_{ij} are the Raman susceptibility components for the modes, $p_{m,\gamma}$ are the mode polarities, and ω_m are the mode frequencies.[30] The Raman susceptibilities are found from a sum over the products of the changes in susceptibility resulting from atomic displacements, $\partial\chi^{(1)}_{ij}/\partial\tau_{\kappa,\beta}$, and the modal atomic eigendisplacements, $u_m(\kappa\beta)$, for all atoms (indexed by κ)[30]

$$\alpha^m_{ij} = \sqrt{\Omega_0} \sum_{\kappa,\beta} \frac{\partial\chi^{(1)}_{ij}}{\partial\tau_{\kappa,\beta}} \mathrm{u}_{\mathrm{m}}(\kappa\beta) \tag{4}$$

The mode polarities are given by a similar sum over the products of the Born effective charges, $Z^*_{\kappa,\gamma\beta}$, and the modal atomic eigendisplacements[30]

$$p_{m,\gamma} = \sum_{\kappa,\beta} Z^*_{\kappa,\gamma\beta} \mathrm{u}_{\mathrm{m}}(\kappa\beta) \tag{5}$$

Two quantities central to the DFPT LEO calculations are the linear and second-order nonlinear susceptibilities. Table 2 gives the calculated optical (ε^∞, atomic positions clamped) and static (ε^0, atomic positions unclamped) zero-frequency dielectric constants at the LDA level with and without scissors corrections. The dielectric constants reflect the same conclusions drawn from the calculated dielectric functions previously shown. As expected, the scissors corrections also reduce the dielectric constants and therefore will play a role in the determination of the LEO coefficients. Table 3 provides the LEO nonlinear susceptibilities, given as $d_{ij} = \chi^{(2)}_{ij}/2$ using contracted indices, with and without scissors corrections. Again,

DOI: 10.1021/acs.jpclett.7b03353
J. Phys. Chem. Lett. 2018, 9, 1018−1027

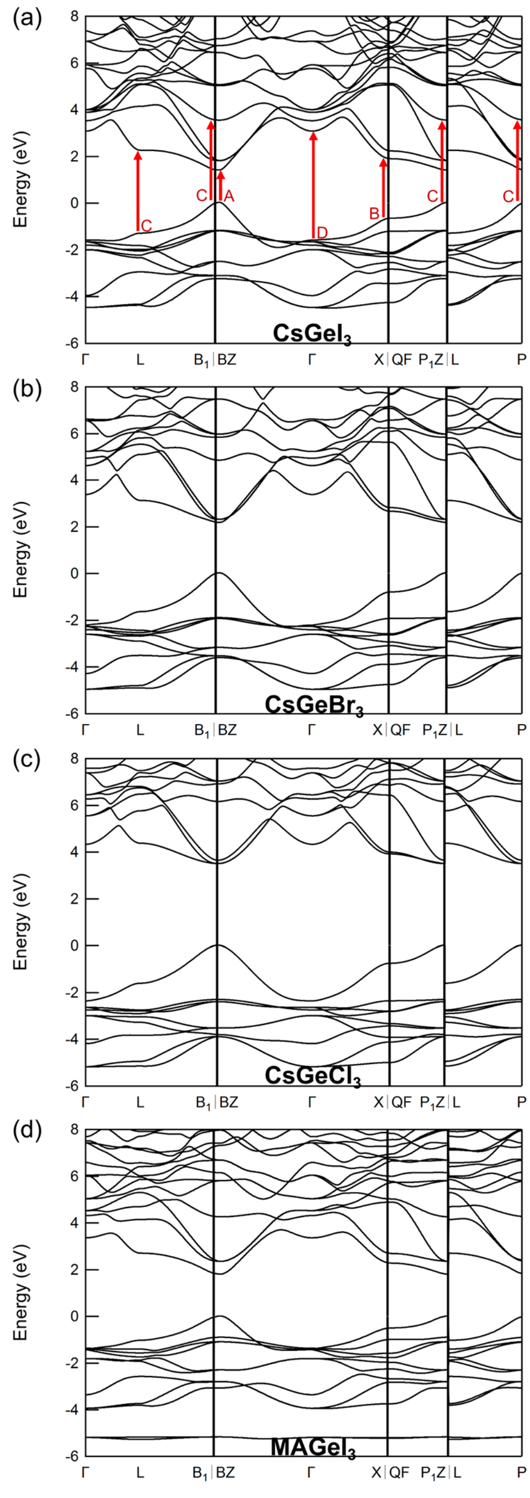

Figure 3. Calculated electronic band diagrams for germanium halide perovskites: (a) $CsGeI_3$, (b) $CsGeBr_3$, (c) $CsGeCl_3$, and (d) $MAGeI_3$. The first few optical transitions have been indicated for $CsGeI_3$. Scissors corrections have been applied, and LDA functionals were used.

the bandgap correction generates a considerable difference. Akin to the linear susceptibilities, the nonlinear susceptibilities increase as the size of the halide anion increases. Substitution of cesium with methylammonium leads to a decrease in the nonlinear susceptibilities. Thus, inspection of all of the compounds shows simply the expected scaling of the nonlinear susceptibility with bandgap.[48] Interestingly, the greatest nonlinear susceptibility component for $CsGeCl_3$ and $CsGeBr_3$ is the d_{33}, while for $CsGeI_3$ and $MAGeI_3$ it is the d_{13}.

Table 2. Optical and Static Linear Dielectric Properties Obtained from $2n + 1$ Theorem DFPT Calculations

compound		$\varepsilon^0_{11,22}$	ε^0_{33}	$\varepsilon^\infty_{11,22}$	ε^∞_{33}
$CsGeCl_3$	LDA	9.87	9.05	3.85	3.69
	SCI	9.32	8.54	3.30	3.18
$CsGeBr_3$	LDA	12.00	11.30	5.07	4.96
	SCI	11.28	10.56	4.34	4.22
$CsGeI_3$	LDA	14.97	14.87	7.48	7.69
	SCI	13.53	13.13	6.04	5.95
$MAGeI_3$	LDA	15.26	7.54	5.36	5.42
	SCI	14.53	6.73	4.63	4.61

Table 3. LEO Nonlinear Susceptibilities ($pm \cdot V^{-1}$) Obtained from $2n + 1$ Theorem DFPT Calculations

compound		d_{11}	d_{13}	d_{33}
$CsGeCl_3$	LDA	1.0	4.6	9.5
	SCI	0.1	2.0	4.8
$CsGeBr_3$	LDA	9.9	16.7	21.6
	SCI	4.1	8.5	12.9
$CsGeI_3$	LDA	104.3	173.4	−32.9
	SCI	33.9	50.6	12.1
$MAGeI_3$	LDA	32.0	44.9	8.9
	SCI	13.6	20.1	10.3

These calculations of the electronic susceptibilities, along with the ionic terms calculated by atomic perturbation calculations, were then used to obtain the LEO coefficients. The space group for the germanium compounds yields eight nonzero tensor components, of which four are unique (Figure S1); these happen to be the same components possessed by $LiNbO_3$. The coefficients for each germanium compound are provided in Table 4. The contributions from each set of ionic transverse optical (TO) phonon modes and from the electronic responses are listed at the LDA level. We have further calculated the final coefficients at two different levels of scissors corrections. The first, SCI1, uses the scissors-corrected dielectric constants. The second, SCI2, uses scissors-corrected values for both the dielectric constants and the nonlinear susceptibilities. We note that this means that we have only used scissors corrections for quantities calculated from electric field perturbations. The differences between the quantities obtained with the different levels of correction illustrate the uncertainty of the calculations; however, considering the available reports of the experimental effective SHG nonlinear susceptibilities for these materials at optical frequencies,[20,22,23] we believe that the more modest values of the LEO susceptibilities obtained with the scissors corrections are more accurate, and therefore, SCI2 stands as the most accurate prediction of the LEO response. We provide a plot to illustrate trends in the electronic and ionic responses with this level of correction in Figure 4. All of the germanium compounds exhibit significant LEO responses; $CsGeI_3$ possesses a component ($r_{51} = 37.64$ $pm \cdot V^{-1}$) that even exceeds the strongest component for $LiNbO_3$ (experimental $r_{33} = 30.8$ $pm \cdot V^{-1}$ at 633 nm;[49] SCI2 calculation 27.28 $pm \cdot V^{-1}$; see Table S2). This is particularly remarkable considering that these calculated values exclude any frequency dependence and therefore represent a lower bound. For the cesium compounds, the LEO response tends to increase as the halide size increases;

DOI: 10.1021/acs.jpclett.7b03353
J. Phys. Chem. Lett. 2018, 9, 1018−1027

Table 4. Clamped Linear EO Coefficients ($pm\cdot V^{-1}$) Obtained from $2n + 1$ Theorem DFPT Calculations[a]

compound	contribution	E modes ω	E modes r_{11}	E modes r_{51}	A_1 modes ω	A_1 modes r_{13}	A_1 modes r_{33}
$CsGeCl_3$	TO1	46	0.75	0.42	43	0.45	−0.64
	TO2	76	−0.08	0.20	66	b	b
	TO3	121	0.20	0.18	148	0.95	1.08
	TO4	213	−6.83	−10.53	253	−5.06	−5.62
	ionic		−5.96	−9.73		−3.66	−5.18
	electronic		−0.27	−1.29		−1.24	−2.80
	total		−6.23	−11.02		−4.90	−7.98
	total (SCI1)		−8.46	−14.90		−6.65	−10.75
	total (SCI2)		−8.14	−13.92		−5.71	−8.88
$CsGeBr_3$	TO1	43	−0.21	−0.78	35	0.10	−0.79
	TO2	53	0.04	0.10	49	b	b
	TO3	79	0.22	0.36	93	0.17	0.25
	TO4	145	−11.47	−18.07	174	−7.72	−8.55
	ionic		−11.42	−18.39		−7.45	−9.09
	electronic		−1.54	−2.65		−2.60	−3.43
	total		−12.96	−21.04		−10.04	−12.52
	total (SCI1)		−17.68	−28.89		−13.70	−17.29
	total (SCI2)		−16.45	−27.12		−11.98	−15.45
$CsGeI_3$	TO1	35	−0.62	−0.88	27	0.28	0.16
	TO2	42	0.00	0.00	39	b	b
	TO3	60	0.61	0.80	70	−0.67	−0.50
	TO4	126	−12.43	−19.94	147	−6.04	−5.67
	ionic		−12.44	−20.02		−6.44	−6.01
	electronic		−7.45	−12.05		−12.39	2.23
	total		−19.89	−32.07		−18.83	−3.79
	total (SCI1)		−30.48	−51.30		−28.85	−6.32
	total (SCI2)		−22.77	−37.64		−15.40	−11.40
$MAGeI_3$	TO1	18	3.00	0.16	15	b	b
	TO2	45	−0.17	−0.26	73	−2.54	−2.25
	TO3	57	0.86	0.98	121	1.60	1.26
	TO4	92	0.19	1.18	124	b	b
	TO5	144	−6.64	−10.99	163	−3.13	−3.16
	TO6	869	0.02	0.02	335	b	b
	TO7	1215	0.00	0.00	1004	0.00	−0.00
	TO8	1431	0.01	0.01	1394	0.00	−0.00
	TO9	1561	−0.00	−0.00	1445	0.04	−0.04
	TO10	2762	0.01	−0.02	2792	−0.01	−0.05
	TO11	2922	−0.00	0.00	2857	0.01	0.00
	ionic		−2.73	−8.91		−4.03	−4.24
	electronic		−4.45	−6.18		−6.24	−1.21
	total		−7.17	−15.09		−10.28	−5.45
	total (SCI1)		−9.62	−20.53		−13.78	−7.52
	total (SCI2)		−6.19	−15.89		−9.16	−7.78

[a]Mode phonon frequencies of ionic contributions are expressed in cm^{-1}. [b]Not Raman-active.

this is primarily driven by the corresponding increases to the electronic contribution. Smaller differences are observed in the ionic contributions. These differences are most noticeable between $CsGeI_3$ and $MAGeI_3$, where the methylammonium compound has a considerably smaller ionic contribution and therefore a much weaker LEO response.

Further insight into the ionic contributions can be gained by inspecting the modal parts and their characteristics. First we consider the Born effective charges (Table S3). The effective charges are defined as the changes in polarization that result from atomic displacements and are factors that control the Coulombic interactions between nuclei.[50,51] They are indicative of the influence of dynamical changes to orbital hybridization caused by atomic displacements.[50,51] For the germanium perovskites, as the size of the halide anion increases, the effective charges deviate more from their nominal charges (A^+, Ge^{2+}, X^-), especially for the Ge and X atoms, indicating that the bonds become more covalent and sensitive to atomic displacements. The vibrational modes involving more covalent bonds would then have a greater electro-optic response. $MAGeI_3$ has bonds with more ionic character than all of the cesium compounds, and the methylammonium cation is almost completely ionized.

Next we consider the characteristics of each mode. The vibrational frequencies of the modes are provided in Table S4, and the modal atomic eigendisplacements are provided in Tables S5−S8. First, we note that the modal frequencies follow an expected Hookean-type relation to the mass of the halide

DOI: 10.1021/acs.jpclett.7b03353
J. Phys. Chem. Lett. 2018, 9, 1018−1027

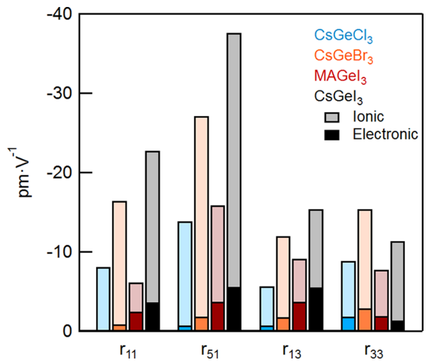

Figure 4. Calculated ionic and electronic LEO responses with scissors-corrected linear and nonlinear susceptibilities (SCI2).

anions, so that the iodide compounds benefit the most from the inverse relation of the electro-optic response to the modal frequency squared. We see that the modes involving the covalent germanium halide bonds and displacements of the germanium atoms possess the greatest electro-optic activity. The displacement of these atoms, having large effective charges, leads to strong modal oscillator strengths (Table S9) and Raman susceptibilities (Tables S10 and S11). These trends then propagate to those observed for the electro-optic activity. Looking at the cesium compounds, the first set of transverse optical modes (modes 4−6, TO1) involves movements of the whole germanium halide octahedra and therefore exhibits weak LEO responses. The second set of transverse optical modes (modes 7−9, TO2) consists of an inactive symmetric mode and a doubly degenerate mode involving small germanium displacements and complex motions of the halide anions; the third set of transverse optical modes (modes 10−12, TO3) involves similar motions as the former's doubly degenerate mode. Altogether, the TO2 and TO3 modes have weak LEO responses. The fourth set of transverse optical modes (modes 13−15, TO4) involves large displacements of the germanium atoms and therefore dominates the ionic LEO response. $MAGeI_3$ has similar vibrational modes as $CsGeI_3$ but also has high-frequency modes relating to the internal degrees of freedom of the methylammonium cations. These additional modes have exceptionally small LEO responses. Furthermore, the strong ionic character of this compound softens the LEO response of the modes involving germanium and halogen movements.

As a complement to our calculations of the LEO coefficients, we have calculated the frequency responses of the SHG and LEO second-order electronic susceptibilities ($\chi^{(2)}_{ijk}(-2\omega;\omega,\omega)$ and $\chi^{(2)}_{ijk}(-\omega;\omega,0)$ respectively). The below-bandgap absolute response curves are provided in Figure 5a−d for the LEO and SHG tensor components of the strongest LEO coefficients and for the effective SHG susceptibilities at the scissors-corrected LDA level. The full frequency responses of the strongest SHG susceptibility tensor components are provided in Figure 5e. The effective SHG susceptibilities rely on all of the tensor components and correspond to the values measurable with powder-SHG experiments. Prior reports of the effective SHG susceptibility at particular wavelengths agree well with our frequency response calculations: $MAGeI_3$ $\chi^{(2)}_{\rm eff}(-2\omega;\omega,\omega)$ = 161 pm·V^{-1} at ∼0.7 eV,[20] $CsGeI_3$ $\chi^{(2)}_{\rm eff}(-2\omega;\omega,\omega)$ = 125 pm·V^{-1} at ∼0.7 eV,[20] $CsGeBr_3$ $\chi^{(2)}_{\rm eff}(-2\omega;\omega,\omega) \approx 18$ pm·V^{-1} at 0.98 eV,[22] and $CsGeCl_3$ $\chi^{(2)}_{\rm eff}(-2\omega;\omega,\omega) \approx 2$ pm·V^{-1} at 0.98 eV.[22] This agreement also justifies the necessity of the scissors corrections (see Figure S2). The LEO susceptibilities display frequency dependence that translates to dependence in the electronic contributions of the LEO coefficients (Figure 5f). Accounting for this and the linear susceptibility dispersion, the r_{51} LEO coefficient of $CsGeI_3$ will then increase to 47 pm·V^{-1} at the telecommunications band of 1550 nm.

In summary, we have determined that the germanium halide perovskites exhibit significant electro-optic responses that for some compounds are on par with or even exceed that of the archetypal electro-optic material $LiNbO_3$. The intrinsically distorted nature of the structures leads to nonlinear electronic susceptibilities and dynamics of the germanium and halogen atoms that drive the electro-optic activity. The nonlinear susceptibilities and electro-optic responses are strongest for the iodide compounds and scale with bandgap. The ionic contributions to the electro-optic characteristics are strongly

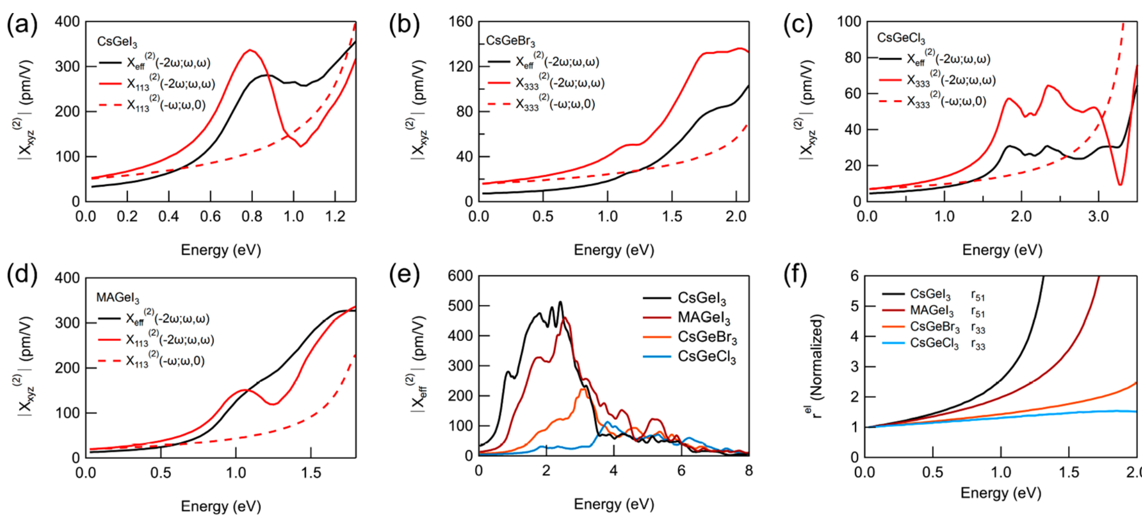

Figure 5. Calculated frequency response of the electronic nonlinear susceptibility. Below-bandgap responses for the effective SHG susceptibility and the SHG and LEO susceptibilities for the strongest LEO tensor components for (a) $CsGeI_3$, (b) $CsGeBr_3$, (c) $CsGeCl_3$, and (d) $MAGeI_3$. (e) Full frequency responses of the effective SHG susceptibility. (f) Normalized frequency response of the strongest electronic LEO terms for each germanium compound. Calculations were done at the level of the LDA and have been scissors-corrected.

DOI: 10.1021/acs.jpclett.7b03353
J. Phys. Chem. Lett. 2018, 9, 1018−1027

influenced by the covalency of the germanium halide bonds and the vibrational properties of the germanium and halogen atoms. Substitution of cesium with methylammonium is detrimental to the ionic response as the bonds become more ionic and the internal vibrations of methylammonium do not contribute. The strong electro-optic performance of the germanium halide perovskites, compounded by their solution-processability, makes them attractive candidates for use in optical modulators.

The realization of germanium halide perovskite optical modulators requires surmounting of a number of experimental challenges. Crystallization techniques must be developed for these materials that produce high-quality macroscopic single crystals. Bulk characterization and implementation in a practical modulator will require approximately an order of magnitude increase in crystal dimensions over the crystals produced from known techniques, which possess dimensions less than 100 μm.[20,28] As well, the crystals must also be of high optical quality in order to prevent any influence of internal or surface scattering on the optical characterization. Recent advances in crystallizing the broader spectrum of metal halide perovskites suggest promising avenues.[14,52−55] Techniques must also be developed for the deposition or growth of the crystals on a modulator platform. The crystals will need to be precisely oriented with the device architecture and have excellent high optical quality in order to maximize the device efficiency. Again, recent reports on lead halide perovskites are encouraging in this regard.[56−60] The present study may help to motivate future endeavors to advance the crystallization and deposition techniques of the germanium halide perovskites with the aim of developing optical modulators.

■ COMPUTATIONAL METHODS

Calculations of the nonlinear response functions were done within density functional perturbation theory, employing the $2n + 1$ theorem, as developed by Veithen et al.[30] and implemented in the ABINIT software package.[61−66] The package can currently only implement nonlinear response function calculations in the Local Density Approximation (LDA) with norm-conserving pseudopotentials. These calculations include the static and optical dielectric constants, the nonlinear optical coefficients, the electro-optic coefficients, and the quantities required in their derivation. Self-consistent calculations were done in the LDA with the exchange−correlation functional Perdew−Wang 92 parametrization.[67] Norm-conserving pseudopotentials generated using the Troullier−Martins method[68] were used. Calculations were done with the experimental lattice constants and with atomic positions relaxed such that maximal forces were less than 10^{-6} Ha·bohr^{-1}. Where indicated, a scissors correction has been applied for all calculations to account for the LDA underestimation of the bandgap and consequent overestimation of the dielectric properties. The scissors corrections have been included at two different levels: SCI1, which includes scissors-corrected dielectric constants, and, SCI2, which includes scissors-corrected dielectric constants and nonlinear susceptibilities. The Brillouin zone was sampled using a Monkhorst−Pack 18 × 18 × 18 grid of special k-points, and wave functions were expanded in plane-waves up to a kinetic energy cutoff of 60 Ha. These parameters were found to be necessary for convergence of the electro-optic coefficients. The calculations of the electro-optic coefficients were benchmarked against calculations for $LiNbO_3$, which are provided in Table S2. These results agree well with prior DFT calculations[30] and with experimental findings.[49]

The frequency-dependent optical responses were calculated with the ABINIT[61−66] package Optic following work by Hughes and Sipe,[35] which uses the independent particle approximation. These calculations include the dielectric function $\varepsilon(\omega)$, the second-harmonic generation (SHG) susceptibility $\chi^{(2)}(-2\omega;\omega,\omega)$, and the LEO susceptibility $\chi^{(2)}(0;\omega,\omega)$. The LEO susceptibility is calculated in the clamped-lattice approximation, which corresponds to the intermediate frequency regime where lattice vibrations are frozen out and electronic dispersion can be neglected. Self-consistent calculations were done in the LDA with the exchange−correlation functional Perdew−Wang 92 parametrization.[67] Norm-conserving pseudopotentials generated using the Troullier−Martins method[68] were used. Calculations were done with the experimental lattice constants and with atomic positions relaxed such that maximal forces were less than 10^{-6} Ha·bohr^{-1}. A scissors correction has been applied for all calculations to account for the LDA underestimation of the bandgap. The Brillouin zone was sampled using a Monkhorst−Pack 26 × 26 × 26 grid of special k-points, wave functions were expanded in plane-waves up to a kinetic energy cutoff of 20 Ha, and the number of bands included was 36 for the inorganic compounds and 40 for the methylammonium compound. These parameters were found to be necessary for convergence of the nonlinear susceptibilities. The effective nonlinear coefficients were calculated based on relations provided by Kurtz and Perry.[69]

Band structure calculations were conducted through ABINIT using the same parameters as in the preceding paragraph. The Brillouin zone was sampled following a k-path for rhombohedral structures as described in ref 70.

Hybrid DFT calculations of the bandgaps were done with the Quantum Espresso[71] implementation package. Norm-conserving pseudopotentials with Perdew−Burke−Ernzerhof[72] exchange−correlations generated with the Martins−Troullier method[68] were combined with HSE06 hybrid functionals,[73,74] and 0.25 exchange fractions and 0.106 screening parameters were used. Lattice constants and atomic positions were simultaneously relaxed, such that forces were less than 2×10^{-6} Ha·bohr^{-1} and pressures were less than 0.5 kbar, prior to hybrid calculations. An 8 × 8 × 8 Monkhorst−Pack k-point grid and 2 × 2 × 2 q-point grid were used with an energy cutoff of 30 Ha for the hybrid calculations.

Atomic illustrations were produced with the visualization software VESTA.[75]

■ ASSOCIATED CONTENT

Supporting Information

The Supporting Information is available free of charge on the ACS Publications website at DOI: 10.1021/acs.jpclett.7b03353.

Imaginary components of the SHG susceptibility, structural parameters following relaxation, lithium niobate benchmark, Born effective charges, atomic eigendisplacements, phonon frequencies, mode oscillator strengths, mode effective charges, and modal Raman susceptibilities (PDF)

■ AUTHOR INFORMATION

Corresponding Author

*E-mail: ted.sargent@utoronto.ca.

ORCID

Grant Walters: 0000-0002-9005-2335

Notes

The authors declare no competing financial interest.

■ ACKNOWLEDGMENTS

The work presented in this publication was supported by funding from an award (KUS-11-009-21) from the King Abdullah University of Science and Technology, the Ontario Research Fund, the Ontario Research Fund Research Excellence Program, and the Natural Sciences and Engineering Research Council (NSERC) of Canada. Computations were performed on the General Purpose Cluster supercomputer at the SciNet HPC Consortium. SciNet is funded by the Canada Foundation for Innovation under the auspices of Compute Canada; the Government of Ontario; Ontario Research Fund - Research Excellence; and the University of Toronto. The authors thank O. Voznyy and A. Jain for useful discussions.

■ REFERENCES

(1) Koeber, S.; Palmer, R.; Lauermann, M.; Heni, W.; Elder, D. L.; Korn, D.; Woessner, M.; Alloatti, L.; Koenig, S.; Schindler, P. C.; et al. Femtojoule Electro-Optic Modulation Using a Silicon−Organic Hybrid Device. *Light: Sci. Appl.* **2015**, *4*, e255.

(2) Alloatti, L.; Palmer, R.; Diebold, S.; Pahl, K. P.; Chen, B.; Dinu, R.; Fournier, M.; Fedeli, J.-M.; Zwick, T.; Freude, W.; et al. 100 GHz Silicon−organic Hybrid Modulator. *Light: Sci. Appl.* **2014**, *3*, e173.

(3) Yang, W. S.; Park, B.-W.; Jung, E. H.; Jeon, N. J.; Kim, Y. C.; Lee, D. U.; Shin, S. S.; Seo, J.; Kim, E. K.; Noh, J. H.; et al. Iodide Management in Formamidinium-Lead-Halide−based Perovskite Layers for Efficient Solar Cells. *Science* **2017**, *356* (6345), 1376−1379.

(4) Jia, Y.; Kerner, R. A.; Grede, A. J.; Rand, B. P.; Giebink, N. C. Continuous-Wave Lasing in an Organic−inorganic Lead Halide Perovskite Semiconductor. *Nat. Photonics* **2017**, *11* (12), 784−788.

(5) Xiao, Z.; Kerner, R. A.; Zhao, L.; Tran, N. L.; Lee, K. M.; Koh, T.-W.; Scholes, G. D.; Rand, B. P. Efficient Perovskite Light-Emitting Diodes Featuring Nanometre-Sized Crystallites. *Nat. Photonics* **2017**, *11* (2), 108−115.

(6) Yuan, M.; Quan, L. N.; Comin, R.; Walters, G.; Sabatini, R.; Voznyy, O.; Hoogland, S.; Zhao, Y.; Beauregard, E. M.; Kanjanaboos, P.; et al. Perovskite Energy Funnels for Efficient Light-Emitting Diodes. *Nat. Nanotechnol.* **2016**, *11* (10), 872−877.

(7) Liao, Y.; Liu, H.; Zhou, W.; Yang, D.; Shang, Y.; Shi, Z.; Li, B.; Jiang, X.; Zhang, L.; Quan, L. N.; et al. Highly Oriented Low-Dimensional Tin Halide Perovskites with Enhanced Stability and Photovoltaic Performance. *J. Am. Chem. Soc.* **2017**, *139* (19), 6693−6699.

(8) Li, W.; Wang, Z.; Deschler, F.; Gao, S.; Friend, R. H.; Cheetham, A. K. Chemically Diverse and Multifunctional Hybrid Organic−inorganic Perovskites. *Nat. Rev. Mater.* **2017**, *2* (3), 16099.

(9) Protesescu, L.; Yakunin, S.; Bodnarchuk, M. I.; Krieg, F.; Caputo, R.; Hendon, C. H.; Yang, R. X.; Walsh, A.; Kovalenko, M. V. Nanocrystals of Cesium Lead Halide Perovskites ($CsPbX_3$, X = Cl, Br, and I): Novel Optoelectronic Materials Showing Bright Emission with Wide Color Gamut. *Nano Lett.* **2015**, *15* (6), 3692−3696.

(10) Kovalenko, M. V.; Protesescu, L.; Bodnarchuk, M. I. Properties and Potential Optoelectronic Applications of Lead Halide Perovskite Nanocrystals. *Science* **2017**, *358* (6364), 745−750.

(11) Weidman, M. C.; Seitz, M.; Stranks, S. D.; Tisdale, W. A. Highly Tunable Colloidal Perovskite Nanoplatelets through Variable Cation, Metal, and Halide Composition. *ACS Nano* **2016**, *10* (8), 7830−7839.

(12) Jeon, N. J.; Noh, J. H.; Kim, Y. C.; Yang, W. S.; Ryu, S.; Seok, S. I. Solvent Engineering for High-Performance Inorganic−organic Hybrid Perovskite Solar Cells. *Nat. Mater.* **2014**, *13* (9), 897−903.

(13) Shi, D.; Adinolfi, V.; Comin, R.; Yuan, M.; Alarousu, E.; Buin, A.; Chen, Y.; Hoogland, S.; Rothenberger, A.; Katsiev, K.; et al. Low Trap-State Density and Long Carrier Diffusion in Organolead Trihalide Perovskite Single Crystals. *Science* **2015**, *347* (6221), 519−522.

(14) Liu, Y.; Yang, Z.; Cui, D.; Ren, X.; Sun, J.; Liu, X.; Zhang, J.; Wei, Q.; Fan, H.; Yu, F.; et al. Two-Inch-Sized Perovskite $CH_3NH_3PbX_3$ (X = Cl, Br, I) Crystals: Growth and Characterization. *Adv. Mater.* **2015**, *27* (35), 5176−5183.

(15) Galy, J.; Meunier, G.; et al. Stereochimie Des Elements Comportant Des Paires Non Liess: Ge (II), As (III), Se (IV), Br (V), Sn (II), Sb (III), Te (IV), I (V), Xe (VI), Tl (I), Pb (II), et Bi (III) (Oxydes, Fluorures et Oxyfluorures). *J. Solid State Chem.* **1975**, *13*, 142−159.

(16) Krishnamoorthy, T.; Ding, H.; Yan, C.; Leong, W. L.; Baikie, T.; Zhang, Z.; Sherburne, M.; Li, S.; Asta, M.; Mathews, N.; et al. Lead-Free Germanium Iodide Perovskite Materials for Photovoltaic Applications. *J. Mater. Chem. A* **2015**, *3* (47), 23829−23832.

(17) Sun, P.-P.; Li, Q.-S.; Yang, L.-N.; Li, Z.-S. Theoretical Insights into a Potential Lead-Free Hybrid Perovskite: Substituting Pb $^{2+}$ with Ge $^{2+}$. *Nanoscale* **2016**, *8* (3), 1503−1512.

(18) Zhao, Y.-Q.; Liu, B.; Yu, Z.-L.; Cao, D.; Cai, M.-Q. Tuning Charge Carrier Types, Superior Mobility and Absorption in Lead-Free Perovskite $CH_3NH_3GeI_3$: Theoretical Study. *Electrochim. Acta* **2017**, *247*, 891−898.

(19) Roknuzzaman, M.; Ostrikov, K.; Wang, H.; Du, A.; Tesfamichael, T. Towards Lead-Free Perovskite Photovoltaics and Optoelectronics by Ab-Initio Simulations. *Sci. Rep.* **2017**, *7*, 14025.

(20) Stoumpos, C. C.; Frazer, L.; Clark, D. J.; Kim, Y. S.; Rhim, S. H.; Freeman, A. J.; Ketterson, J. B.; Jang, J. I.; Kanatzidis, M. G. Hybrid Germanium Iodide Perovskite Semiconductors: Active Lone Pairs, Structural Distortions, Direct and Indirect Energy Gaps, and Strong Nonlinear Optical Properties. *J. Am. Chem. Soc.* **2015**, *137* (21), 6804−6819.

(21) Huang, C. B.; Wang, Z. Y.; Wu, H. X.; Ni, Y. B.; Xiao, R. C.; Qi, M. Ab Initio Study of the Linear and Nonlinear Optical Properties of Hexagonal CdSe. *Comput. Condens. Matter* **2015**, *3*, 41−45.

(22) Lin, Z.-G.; Tang, L.-C.; Chou, C.-P. Study on Mid-IR NLO Crystals $CsGe(Br_xCl_{1-x})_3$. *Opt. Mater.* **2008**, *31* (1), 28−34.

(23) Lin, Z.-G.; Tang, L.-C.; Chou, C.-P. Characterization and Properties of Infrared NLO Crystals: $AGeX_3$ (A = Rb, Cs; X = Cl, Br). *J. Cryst. Growth* **2008**, *310* (13), 3224−3229.

(24) Kang, L.; Ramo, D. M.; Lin, Z.; Bristowe, P. D.; Qin, J.; Chen, C. First Principles Selection and Design of Mid-IR Nonlinear Optical Halide Crystals. *J. Mater. Chem. C* **2013**, *1* (44), 7363.

(25) Qing-tian, G.; Chang-shui, F.; Yong-sheng, L.; Xiang-wen, W.; Qi-wei, P.; Wei, S. Growth and Properties of $CsGeCl_3$ Single Crystal. *Integr. Ferroelectr.* **2001**, *35* (1−4), 41−46.

(26) Lin, Z.-G.; Tang, L.-C.; Chou, C.-P. Infrared Properties of $CsGe(Br_xCl_{1-x})_3$, Nonlinear Optical Rhombohedral Semiconductor. *J. Phys.: Condens. Matter* **2007**, *19*, 476209.

(27) Schwarz, U.; Hillebrecht, H.; Kaupp, M.; Syassen, K.; von Schnering, H.-G.; et al. Pressure-Induced Phase Transition in $CsGeBr_3$ Studied by X-Ray Diffraction and Raman Spectroscopy. *J. Solid State Chem.* **1995**, *118*, 20−27.

(28) Qing-Tian, G.; Chang-Shui, F.; Wei, S.; Xiang-Wen, W.; Qi-Wei, P. New Wide-Band Nonlinear Optics $CsGeCl_3$ Crystal. *J. Cryst. Growth* **2001**, *225* (2), 501−504.

(29) Tang, L. C.; Huang, J. Y.; Chang, C. S.; Lee, M. H.; Liu, L. Q. New Infrared Nonlinear Optical Crystal $CsGeBr_3$: Synthesis, Structure and Powder Second-Harmonic Generation Properties. *J. Phys.: Condens. Matter* **2005**, *17* (46), 7275−7286.

(30) Veithen, M.; Gonze, X.; Ghosez, P. Nonlinear Optical Susceptibilities, Raman Efficiencies, and Electro-Optic Tensors from First-Principles Density Functional Perturbation Theory. *Phys. Rev. B: Condens. Matter Mater. Phys.* **2005**, *71*, 125107.

(31) Sando, D.; Hermet, P.; Allibe, J.; Bourderionnet, J.; Fusil, S.; Carrétéro, C.; Jacquet, E.; Mage, J.-C.; Dolfi, D.; Barthélémy, A.; et al. Linear Electro-Optic Effect in Multiferroic $BiFeO_3$ Thin Films. *Phys. Rev. B: Condens. Matter Mater. Phys.* **2014**, *89*, 195106.

(32) Djani, H.; Hermet, P.; Ghosez, P. First-Principles Characterization of the $P2_1ab$ Ferroelectric Phase of Aurivillius Bi_2WO_6. *J. Phys. Chem. C* **2014**, *118* (25), 13514−13524.

DOI: 10.1021/acs.jpclett.7b03353
J. Phys. Chem. Lett. 2018, 9, 1018−1027

(33) Chen, Z.-X.; Chen, Y.; Jiang, Y.-S. DFT Study on Ferroelectricity of $BaTiO_3$. *J. Phys. Chem. B* **2001**, *105* (24), 5766−5771.
(34) Wang, C.-Y.; Guo, G.-Y. Nonlinear Optical Properties of Transition-Metal Dichalcogenide MX_2 (M= Mo, W; X= S, Se) Monolayers and Trilayers from First-Principles Calculations. *J. Phys. Chem. C* **2015**, *119* (23), 13268−13276.
(35) Hughes, J. L.; Sipe, J. E. Calculation of Second-Order Optical Response in Semiconductors. *Phys. Rev. B: Condens. Matter Mater. Phys.* **1996**, *53* (16), 10751.
(36) Levine, Z. H.; Allan, D. C. Linear Optical Response in Silicon and Germanium Including Self-Energy Effects. *Phys. Rev. Lett.* **1989**, *63* (16), 1719.
(37) Levine, Z. H.; Allan, D. C. Calculation of the Nonlinear Susceptibility for Optical Second-Harmonic Generation in III-V Semiconductors. *Phys. Rev. Lett.* **1991**, *66* (1), 41.
(38) Levine, Z. H.; Allan, D. C. Quasiparticle Calculation of the Dielectric Response of Silicon and Germanium. *Phys. Rev. B: Condens. Matter Mater. Phys.* **1991**, *43* (5), 4187.
(39) Hughes, J. L.; Wang, Y.; Sipe, J. E. Calculation of Linear and Second-Order Optical Response in Wurtzite GaN and AlN. *Phys. Rev. B: Condens. Matter Mater. Phys.* **1997**, *55* (20), 13630.
(40) Zheng, F.; Tao, J.; Rappe, A. M. Frequency-Dependent Dielectric Function of Semiconductors with Application to Physisorption. *Phys. Rev. B: Condens. Matter Mater. Phys.* **2017**, *95*, 35203.
(41) Van Troeye, B.; Gillet, Y.; Poncé, S.; Gonze, X. First-Principles Characterization of the Electronic and Optical Properties of Hexagonal $LiIO_3$. *Opt. Mater.* **2014**, *36* (9), 1494−1501.
(42) Song, J.-H.; Freeman, A. J.; Bera, T. K.; Chung, I.; Kanatzidis, M. G. First-Principles Prediction of an Enhanced Optical Second-Harmonic Susceptibility of Low-Dimensional Alkali-Metal Chalcogenides. *Phys. Rev. B: Condens. Matter Mater. Phys.* **2009**, *79*, 245203.
(43) Reshak, A. H.; Atuchin, V. V.; Auluck, S.; Kityk, I. V. First and Second Harmonic Generation of the Optical Susceptibilities for the Non-Centro-Symmetric Orthorhombic $AgCd_2$ GaS_4. *J. Phys.: Condens. Matter* **2008**, *20* (32), 325234.
(44) Kong, F.; Jiang, G. Nonlinear Optical Response of Wurtzite ZnO from First Principles. *Phys. B* **2009**, *404* (16), 2340−2344.
(45) Reshak, A. H.; Auluck, S.; Kityk, I. V. Specific Features in the Band Structure and Linear and Nonlinear Optical Susceptibilities of $La_2CaB_{10}O_{19}$ Crystals. *Phys. Rev. B: Condens. Matter Mater. Phys.* **2007**, *75*, 245120.
(46) Li, Z.; Liu, Q.; Wang, Y.; Iitaka, T.; Su, H.; Tohyama, T.; Yang, Z.; Pan, S. Second-Harmonic Generation in Noncentrosymmetric Phosphates. *Phys. Rev. B: Condens. Matter Mater. Phys.* **2017**, *96*, 35205.
(47) Huang, L.; Lambrecht, W. R. L. Electronic Band Structure Trends of Perovskite Halides: Beyond Pb and Sn to Ge and Si. *Phys. Rev. B: Condens. Matter Mater. Phys.* **2016**, *93*, 195211.
(48) Jackson, A. G.; Ohmer, M. C.; LeClair, S. R. Relationship of the Second Order Nonlinear Optical Coefficient to Energy Gap in Inorganic Non-Centrosymmetric Crystals. *Infrared Phys. Technol.* **1997**, *38* (4), 233−244.
(49) Yariv, A.; Yeh, P. *Photonics: Optical Electronics in Modern Communications*, 6th ed.; Oxford University: New York, 2007.
(50) Ghosez, P.; Michenaud, J.-P.; Gonze, X. Dynamical Atomic Charges: The Case of ABO_3 Compounds. *Phys. Rev. B: Condens. Matter Mater. Phys.* **1998**, *58* (10), 6224.
(51) Marek, V. First-Principles Study of Ferroelectric Oxides: Dynamical Properties and Electron Localization Tensor. *DEA Thesis*; University of Liege: Leige, Belgium, 2003.
(52) Peng, W.; Yin, J.; Ho, K.-T.; Ouellette, O.; De Bastiani, M.; Murali, B.; El Tall, O.; Shen, C.; Miao, X.; Pan, J.; et al. Ultralow Self-Doping in Two-Dimensional Hybrid Perovskite Single Crystals. *Nano Lett.* **2017**, *17* (8), 4759−4767.
(53) Dang, Y.; Zhou, Y.; Liu, X.; Ju, D.; Xia, S.; Xia, H.; Tao, X. Formation of Hybrid Perovskite Tin Iodide Single Crystals by Top-Seeded Solution Growth. *Angew. Chem., Int. Ed.* **2016**, *55* (10), 3447−3450.
(54) Saidaminov, M. I.; Abdelhady, A. L.; Maculan, G.; Bakr, O. M. Retrograde Solubility of Formamidinium and Methylammonium Lead Halide Perovskites Enabling Rapid Single Crystal Growth. *Chem. Commun.* **2015**, *51* (100), 17658−17661.
(55) Dang, Y.; Liu, Y.; Sun, Y.; Yuan, D.; Liu, X.; Lu, W.; Liu, G.; Xia, H.; Tao, X. Bulk Crystal Growth of Hybrid Perovskite Material $CH_3NH_3PbI_3$. *CrystEngComm* **2015**, *17* (3), 665−670.
(56) Lee, L.; Baek, J.; Park, K. S.; Lee, Y.-E.; Shrestha, N. K.; Sung, M. M. Wafer-Scale Single-Crystal Perovskite Patterned Thin Films Based on Geometrically-Confined Lateral Crystal Growth. *Nat. Commun.* **2017**, *8*, 15882.
(57) Feng, J.; Yan, X.; Zhang, Y.; Wang, X.; Wu, Y.; Su, B.; Fu, H.; Jiang, L. Liquid Knife" to Fabricate Patterning Single-Crystalline Perovskite Microplates toward High-Performance Laser Arrays. *Adv. Mater.* **2016**, *28* (19), 3732−3741.
(58) Wang, G.; Li, D.; Cheng, H.-C.; Li, Y.; Chen, C.-Y.; Yin, A.; Zhao, Z.; Lin, Z.; Wu, H.; He, Q.; et al. Wafer-Scale Growth of Large Arrays of Perovskite Microplate Crystals for Functional Electronics and Optoelectronics. *Sci. Adv.* **2015**, *1*, e1500613.
(59) Spina, M.; Bonvin, E.; Sienkiewicz, A.; Forró, L.; Horváth, E.; et al. Controlled Growth of CH3NH3PbI3 Nanowires in Arrays of Open Nanofluidic Channels. *Sci. Rep.* **2016**, *6*, 19834.
(60) Cho, N.; Li, F.; Turedi, B.; Sinatra, L.; Sarmah, S. P.; Parida, M. R.; Saidaminov, M. I.; Murali, B.; Burlakov, V. M.; Goriely, A.; et al. Pure Crystal Orientation and Anisotropic Charge Transport in Large-Area Hybrid Perovskite Films. *Nat. Commun.* **2016**, *7*, 13407.
(61) Gonze, X.; Jollet, F.; Abreu Araujo, F.; Adams, D.; Amadon, B.; Applencourt, T.; Audouze, C.; Beuken, J.-M.; Bieder, J.; Bokhanchuk, A.; et al. Recent Developments in the ABINIT Software Package. *Comput. Phys. Commun.* **2016**, *205*, 106−131.
(62) Gonze, X.; Amadon, B.; Anglade, P.-M.; Beuken, J.-M.; Bottin, F.; Boulanger, P.; Bruneval, F.; Caliste, D.; Caracas, R.; Côté, M.; et al. ABINIT: First-Principles Approach to Material and Nanosystem Properties. *Comput. Phys. Commun.* **2009**, *180* (12), 2582−2615.
(63) Gonze, X.; Rignanese, G.-M.; Verstraete, M. J.; Beuken, J.-M.; Pouillon, Y.; Caracas, R.; Jollet, F.; Torrent, M.; Zerah, G.; Mikami, M.; et al. A Brief Introduction to the ABINIT Software Package. *Z. Kristallogr. - Cryst. Mater.* **2005**, *220*, 558−562.
(64) Gonze, X.; Beuken, J.-M.; Caracas, R.; Detraux, F.; Fuchs, M.; Rignanese, G.-M.; Sindic, L.; Verstraete, M.; Zerah, G.; Jollet, F.; et al. First-Principles Computation of Material Properties: The ABINIT Software Project. *Comput. Mater. Sci.* **2002**, *25* (3), 478−492.
(65) Gonze, X. First-Principles Responses of Solids to Atomic Displacements and Homogeneous Electric Fields: Implementation of a Conjugate-Gradient Algorithm. *Phys. Rev. B: Condens. Matter Mater. Phys.* **1997**, *55* (16), 10337.
(66) Gonze, X.; Lee, C. Dynamical Matrices, Born Effective Charges, Dielectric Permittivity Tensors, and Interatomic Force Constants from Density-Functional Perturbation Theory. *Phys. Rev. B: Condens. Matter Mater. Phys.* **1997**, *55* (16), 10355.
(67) Perdew, J. P.; Wang, Y. Accurate and Simple Analytic Representation of the Electron-Gas Correlation Energy. *Phys. Rev. B: Condens. Matter Mater. Phys.* **1992**, *45* (23), 13244−13249.
(68) Troullier, N.; Martins, J. L. Efficient Pseudopotentials for Plane-Wave Calculations. *Phys. Rev. B: Condens. Matter Mater. Phys.* **1991**, *43* (3), 1993.
(69) Kurtz, S. K.; Perry, T. T. A Powder Technique for the Evaluation of Nonlinear Optical Materials. *J. Appl. Phys.* **1968**, *39* (8), 3798−3813.
(70) Setyawan, W.; Curtarolo, S. High-Throughput Electronic Band Structure Calculations: Challenges and Tools. *Comput. Mater. Sci.* **2010**, *49* (2), 299−312.
(71) Giannozzi, P.; Baroni, S.; Bonini, N.; Calandra, M.; Car, R.; Cavazzoni, C.; Ceresoli, D.; Chiarotti, G. L.; Cococcioni, M.; Dabo, I.; et al. QUANTUM ESPRESSO: A Modular and Open-Source Software Project for Quantum Simulations of Materials. *J. Phys.: Condens. Matter* **2009**, *21* (39), 395502.

DOI: 10.1021/acs.jpclett.7b03353
J. Phys. Chem. Lett. 2018, 9, 1018−1027

(72) Perdew, J. P.; Burke, K.; Ernzerhof, M. Generalized Gradient Approximation Made Simple. *Phys. Rev. Lett.* **1996**, *77* (18), 3865−3868.
(73) Heyd, J.; Scuseria, G. E.; Ernzerhof, M. Hybrid Functionals Based on a Screened Coulomb Potential. *J. Chem. Phys.* **2003**, *118* (18), 8207−8215.
(74) Heyd, J.; Scuseria, G. E.; Ernzerhof, M. Erratum: "Hybrid Functionals Based on a Screened Coulomb Potential" [J. Chem. Phys. 118, 8207 (2003)]. *J. Chem. Phys.* **2006**, *124* (21), 219906.
(75) Momma, K.; Izumi, F. *VESTA 3* for Three-Dimensional Visualization of Crystal, Volumetric and Morphology Data. *J. Appl. Crystallogr.* **2011**, *44* (6), 1272−1276.

DOI: 10.1021/acs.jpclett.7b03353
J. Phys. Chem. Lett. 2018, 9, 1018−1027